Cumulative fatigue damage in thin aluminum films evaluated non-destructively with lasers via zero-group-velocity Lamb modes

Guqi Yan, Samuel Raetz *, Nikolay Chigarev, James Blondeau, Vitalyi E. Gusev, Vincent Tournat *

Laboratoire d'Acoustique de l'Université du Mans (LAUM), UMR 6613, Institut d'Acoustique - Graduate School (IA-GS), CNRS, Le Mans Université, France

ARTICLE INFO

ABSTRACT

In this paper, a non-contact non-destructive evaluation of cumulative fatigue damage in 75 μm-thick aluminum plates is conducted by using the first symmetric zero-group-velocity Lamb mode and taking benefit of its local and long-lasting resonance feature. The tested aluminum sheets are subjected to fatigue loading, in a two sides clamped compression configuration inducing buckling. For understanding the experimental observations, we propose and establish an empirically-inspired theoretical modeling based on the cumulative damage theory, completed with a finite element simulation, for comparison with the experimental measurements. The observed phenomena along fatigue cycles show the potential for the prediction of the fatigue lifetime and the quantitative assessment of different stages of the fatigue damage in solid plate structures. Good agreement is found between the proposed theory/simulation and the experiment on zero-group-velocity resonance frequency. The quality factor of zero-group-velocity resonance is also experimentally studied and compared with numerical calculations, a disagreement is observed after ∼30% of fatigue lifetime. This point elucidates the start time of the change of mechanical properties during the early fatigue stage and is identified as a potential path for the improvement of the proposed empirical model in the future.

1. Introduction

Material life time prediction, and more specifically, the progressive fatigue failure prediction, is indeed always one of the key foundations of safety of the serving equipments, and it is also an important aspect of modern mechanical design and manufacture [1–5]. As a commonly utilized machine component, solid plate structures, such as metallic sheets, are often subjected to fatigue loads in service of engineering. Therefore, the evaluation of the cumulative fatigue damage in thin metallic films is of importance for lifetime prediction and then for reliability and security of practical engineering equipments/machines with such structures in service. During the last two decades, this scientific importance was repeatedly raised not only in the field of metallic materials but also in the field of other kinds of materials such as the composites [6–12].

For more than 70 years and following the seminal work by Miner [13], a tremendous amount of research has been dedicated to propose theoretical expressions of an index D providing the cumulative fatigue damage in a material subjected to cyclic loading. This index intends to give an estimate of the state of fatigue of the material. To express the fatigue state, different material or nonmaterial parameters could be used, such as: the ratio between the current number of loading cycles and the number of cycles for the failure to occur, the density,

the Young's modulus, the cross-sectional area of the damaged sample, etc. The mathematical expression of the cumulative fatigue damage index not only depends on the chosen parameter but on empirically- or analytically-based assumptions on the fatigue process. For instance, Miner [13] conceptually considered that part of the mechanical energy of the loading is absorbed by the fatigue process at each cycle. The amount of absorbed energy is moreover assumed by Miner to be the same at each cycle, which leads to consider that the cumulative damage linearly increases with the number of cycles, regardless of the loading sequence. This conceptual model has been shown to be limited since the irreversible micro-rupture process associated to D depends nonlinearly on the number of cycles. More realistic models have then been sought. We can cite, for instance, the Lemaitre–Plumtree model [14] that accounts for the fact that, for a strain-controlled cyclic loading, the stress response evolves due to material fatigue, while the Miner's theory states that the response does not evolve. The cumulative damage index in the Lemaitre–Plumtree model therefore depends on a damage exponent, that in turn depends on the material mechanical property and on the strain amplitude of the cyclic loading. We focus here on the Miner's and Lemaitre–Plumtree's theory that we use in the following. For further theories and details, the readers are referred to the numerous review articles on the topic of cumulative fatigue damage, among which the

---

* Corresponding authors.
E-mail addresses: samuel.raetz@univ-lemans.fr (S. Raetz), vincent.tournat@univ-lemans.fr (V. Tournat).

authors would like to enlighten the review articles by Fatemi and Yang [15,16] for their completeness and the important work of method classification allowing a global view of the state of the art of the cumulative damage theory at a glance.

Ultrasonic methods are commonly used in nondestructive testing/evaluation (NDT/E) of fatigued materials: by detecting acoustic nonlinearity, crack length, elasticity, and the accumulation of damage [17–20]. The laser ultrasonic (LU) technique, where both the generation and the detection of ultrasounds are based on lasers, are more and more widely used for NDT/E applications and characterization of physical/mechanical properties of materials [21–24]. The opto-acoustic technique can indeed provide: a large bandwidth thanks to the extremely short laser pulse, a high spatial resolution owing to the possibility of focusing the laser beam down to micrometers. Moreover, the opto-acoustic technique allows the contactless studies of a specimen, which avoids the use of contact transducers [18–20,25–28]. In recent years, zero-group-velocity (ZGV) Lamb modes [29] have proven to be an efficient tool to probe locally and accurately the thickness [30,31] or the mechanical properties of plates [32–34], the anisotropy [35], to inform on the adhesion level [36] as well as to detect defects [37].

Recently, we have demonstrated [38] the ability as well as the reproducibility of the ZGV Lamb mode (introduced in Section 2) for locating the fatigue damage, for predicting the fatigue lifetime, and for assessing the cumulative fatigue damage levels during a fatigue process, thanks to the non-monotonous variation of a ZGV mode frequency during the fatigue process. In this paper, we aim at explaining the experimental observations (Sections 3 and 4) by their comparison with numerical simulations using finite element method (FEM) (Section 5.2) and go deeper in the analysis of the observed processes. An empirical model based on the cumulative damage theory is also proposed here for this purpose. By wrongly (on purpose) assuming that we can numerically reproduce the experimentally-observed variation of the ZGV frequency by accounting only for the thickness decrease of the fatigued plate, we will in particular point out from which stage in the fatigue life the changes of mechanical properties cannot be ignored anymore.

2. ZGV Lamb modes

When a plate structure is excited by a spatially localized impact, multiple Lamb modes can be generated, both symmetrical modes (denoted as S) and anti-symmetrical modes (denoted as A). Among them, there are several specific modes that exhibit an anomalous behavior at frequencies where the group velocity vanishes, while the phase velocity remains finite. The dispersion curves of the Lamb waves for both S (solid red lines) and A (dashed blue lines) Lamb modes are plotted in Fig. 1, for an aluminum plate with a thickness of $2h = 75$ mm, longitudinal wave velocity $V_L = 6450$ m s^{-1} and shear wave velocity $V_T = 3100$ m s^{-1}. In Fig. 1, the first symmetrical zero-group-velocity (ZGV) Lamb mode, the $S_1 S_2$-ZGV mode, is indicated with an arrow. Such a ZGV Lamb mode results from the interference of two guided modes coexisting for a unique couple of frequency/wavenumber. For example, the $S_1 S_2$-ZGV mode can be seen as being composed of the forward propagating S_2 Lamb mode and the backward propagating S_{1b} Lamb mode, where b stands for "backward" and indicates that the phase velocity and group velocity of S_1 mode are of opposite sign in that frequency range [29]. As mentioned above, the ZGV resonance frequency is very sensitive to the local thickness [29–31,39,40] and to the local mechanical properties [33,41] of plates, which both are changing when a sample is subjected to fatigue cycles. Hence, when the mechanical properties of the plate, such as the elastic modulus, the Poisson's ratio, and the density, are not modified, the following relation between the variation Δf of the ZGV frequency f and the variation Δh of the thickness h holds

$$\frac{\Delta f}{f} \cong -\frac{\Delta h}{h}. \tag{1}$$
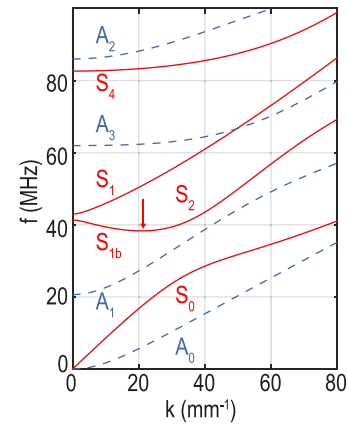

Fig. 1. (Color online) Dispersion relations of Lamb waves for both symmetrical modes (solid red lines) and anti-symmetrical modes (dashed blue lines), the first ZGV mode is indicated by red arrow.

A decrease in the sample thickness with unchanged mechanical properties will therefore lead to a proportional monotonous increase of the ZGV frequency. This relation is an interesting property for NDE applications [37], and it will be used for establishing the empirical model used in the finite element simulation discussed in Section 5. The experimental setup for the LU experiments and the fatigue test configuration are now presented in the next section.

3. Description of the experimental configurations

3.1. Experimental setup for laser ultrasonics measurements

The experimental setup is schematically illustrated in Fig. 2. The pump laser (pulse duration of ∼0.75 ns with a repetition rate of 1 kHz) has an optical wavelength of 1064 nm and was focused into a stretched ellipse (long diameter ∼500 μm and small diameter ∼25 μm), close to a line generation source. This so-called pump laser is locally absorbed by the aluminum plate, therefore creating a local and sudden thermal stress which generates ultrasonic wave propagating within the plate. The continuous probe laser (with a wavelength of 532 nm) is focused to a circular spot (diameter ∼25 μm) in the vicinity (∼20 μm) of the line source and is used for ultrasonic wave detection thanks to the beam deflection technique (denoted by the dashed red rectangular box in Fig. 2), as often used for LU probing [42–44]. The calibration of the overlapping/separation of the generation line source and the detection circular spot is controlled by a rotating dichroic mirror. Note that the distance between the pump laser and the probe laser is mandatory for the detection of the ZGV resonance since the beam-deflection technique is sensitive to the radial gradient of the normal displacement, which is zero for the ZGV mode at the pump laser location. The aluminum plate is attached to a three-dimension translational platform. In this work, only the x-direction translation is used in order to achieve the B-scan measurements as denoted by the double-headed arrow in Fig. 2.

3.2. Fatigue test configuration

In order to fatigue the specimen, a "homemade" fatigue machine using a micro-controlled linear stage has been developed. The chosen fatigue test configuration is a two sides clamped compression inducing buckling as illustrated in Fig. 3(a). The unloaded plate [bottom in Fig. 3(a)] is originally of the length $2L$ with x-axis along the plate surface and z-axis normal to the unloaded plate surface. Each tested aluminum sheet is first subjected to a compression where the plate buckled [top in Fig. 3(a)]: the compression is imposed by moving one of the sides of the fatigue machine where the sample is clamped
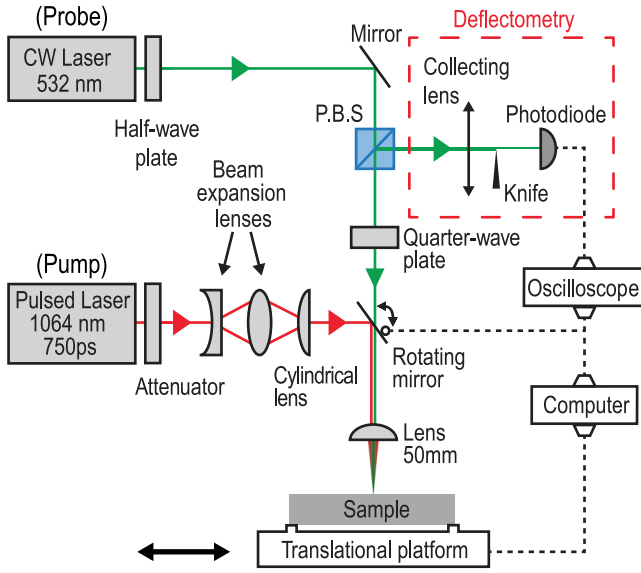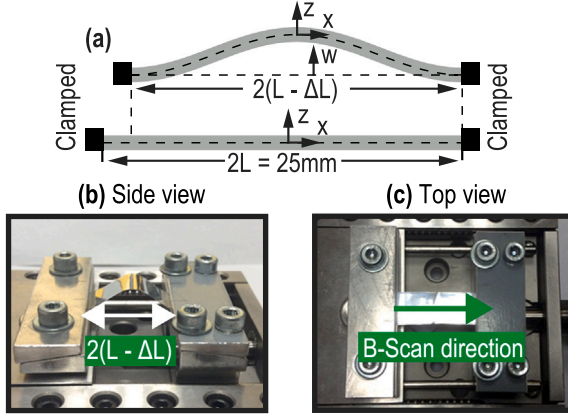
Fig. 2. Experimental setup.

Fig. 3. Fatigue configuration: (a) Illustration of the plate specimen loaded (top) and unloaded (bottom); (b) side-view photo of the loaded specimen; (c) top-view photo of the unloaded specimen.

(the left one in the figure) by $2\Delta L$ along x-axis towards the other side (the right one in the figure). Then a cyclic displacement of the same side (left) is imposed along x-axis, giving rise to the so-called loading cycles, until the specimen failure. Fig. 3(b) shows the side-view photo of the loaded specimen whose profile is similar to a cosine function as shown in Eq. (2). Fig. 3(c) is the top-view picture of the specimen that is unloaded to carry out the opto-acoustic measurements with the setup described in Fig. 2 that needs a flat surface for the B-scan measurements. Note that when the sample is unloaded, it is also straightened by applying a slight traction in order to obtain a flat surface necessary to get a good signal-to-noise ratio with the technique used for the detection (beam-deflection technique). The green arrow in Fig. 3(c) denotes the direction of the scan. The unloading of the sample is performed at regular intervals of fatigue loading cycles in order to follow the change in the ZGV frequency all along the fatigue life of the sample. The normal deflection of a buckled plate can be expressed as [45],

$$w(x) = \frac{\delta}{2} \left[1 + \cos\left(\frac{\pi x}{L - \Delta L}\right) \right], \qquad (2)$$
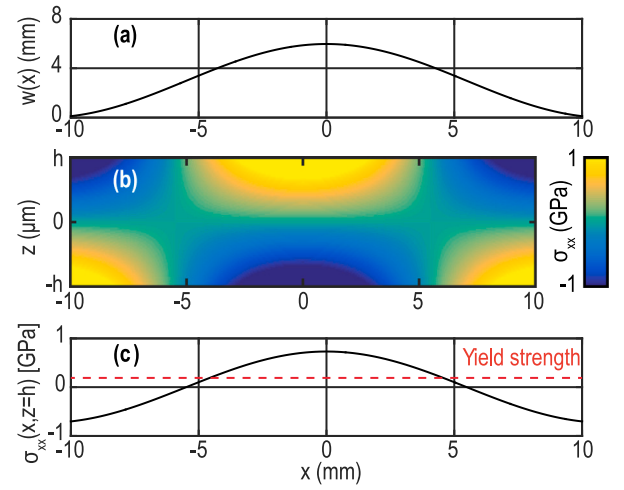
Fig. 4. Buckling of a thin plate: (a) normal deflection of a plate with unloaded length of $2L = 25$ mm and shortening length of $2\Delta L = 5$ mm, (b) space distribution of the cross section stress σ_{xx} in (x, z) plane, and (c) surface stress distribution $\sigma_{xx}(x, h)$ (solid line) and specimen's tensile yield strength (dashed red line).

and the formulation of the stress distribution of a buckled plate is denoted by:

$$\sigma_{xx}(x, z) = \frac{\delta \pi^2 E}{16(1 - \nu^2)(L - \Delta L)^2} z \cos\left[\frac{\pi x}{L - \Delta L}\right], \qquad (3)$$

where $x = 0$ is located in the center of the buckled plate, L is half the length of the plate, ΔL is half the displacement along the x axis of the moving part of the fatigue machine [Fig. 3(a)], and δ is the buckling deflection in the center of the specimen as defined in Refs. [45,46], ν is the Poisson's ratio, E is the Young modulus. For the details on the buckling plate theory, readers are referred to the following references [45–49]. In Fig. 4, the calculated buckled plate deflection with unloaded length of $2L = 25$ mm and shortening length of $2\Delta L = 5$ mm [see Fig. 4(a)], the cross section stress distribution $\sigma_{xx}(x, z)$ [see Fig. 4(b)], and the surface ($z = h$) stress distribution [see Fig. 4(c)] are presented in the case of an aluminum plate (with the properties in Tab. S1, Supplemental Material Note 2). In Fig. 4(c) the dashed horizontal line stands for the tensile yield strength of aluminum [5]. In our experiment, the specimen is unloaded at regular intervals of 500 cycles from the fatigue test system and probed each time using the pump–probe laser technique shown in Fig. 2 to get the values of the $S_1 S_2$-ZGV resonance frequency along the scanning path. This means that for each position during the scanning, an opto-acoustic signal is measured and saved for spectral analysis. For each set of measurements, the scanning length, chosen to be 10 mm, corresponds to the estimated damaged region width, according to the value of the tensile yield strength and the stress distribution calculation [see Fig. 4(c)]. The scan is performed with a step of 100 μm, i.e. 101 points of detection in total. The used motorized actuator provides a 50 mm travel range with a minimum incremental motion of 0.1 μm, which is sufficiently accurate for our measurements. Note that the measurements on the intact specimen are saved as the reference in order to make the comparison with all the other ones after the specimen is damaged.

4. Experimental results and analysis

4.1. Experimental results

In Fig. 5, an example of (a) a received LU temporal signal (processed by a high-pass filter in order to avoid A_0 Lamb mode) and (b) its frequency spectrum (computed over the rectangular time window 0.2 μs to 8 μs) are plotted. A sharp peak at ~38 MHz [see inset in Fig. 5(b)]
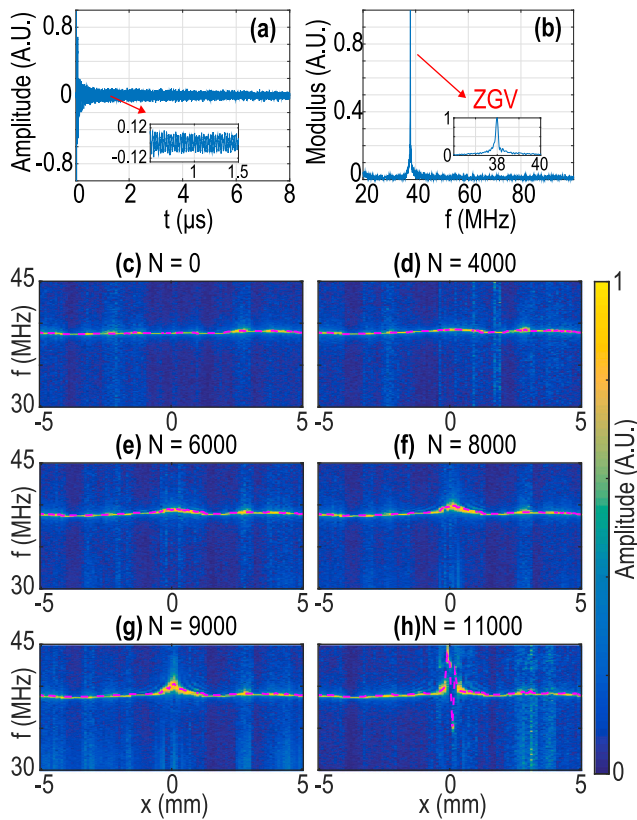
Fig. 5. (a) Example of a received LU temporal signal on the intact specimen ($N = 0$) and (b) its fast Fourier transform (FFT) with a sharp peak corresponding to the $S_1 S_2$-ZGV resonance frequency. Several chosen experimental measurements : amplitude spectrum density as a function of frequency (f) and specimen position (x) for loading cycles (c) $N = 0$, (d) $N = 4000$, (e) $N = 6000$, (f) $N = 8000$, (g) $N = 9000$, and (h) $N = 11,000$.

is observed and corresponds to the $S_1 S_2$-ZGV resonance frequency. Several representative spatial distributions of the Fourier transform (FT) spectrum for different numbers N of fatigue cycles are depicted in Fig. 5(c–h) for the frequency range (y-axis) $[30, 45]$ MHz and the scanning range x (x-axis) $[-5, 5]$ mm. Note that, in Fig. 5(c–h), the FT spectra forming an image are all normalized for each x position by the amplitude of the ZGV peak value. The extracted ZGV frequency values in Fig. 5 are denoted by purple dashed lines. The ZGV frequency values extracted in the intact case [see Fig. 5(c)] are considered as the reference. It is seen that the frequency value is not unique, even in the intact case, and lies in the range $[38.45, 38.66]$ MHz due to the initial thickness variation of the tested plate. The original thickness $2h$ of the intact specimen is therefore determined to lie in the interval $[74.3, 74.7]$ μm. While the number N of fatigue cycles increases, an obvious increase of the ZGV frequency is observed in the center of the measurements (maximum increase at x = 0.1 mm) [see Fig. 5(d)–(h)]. After ~10,500 fatigue cycles, a decrease of the ZGV frequency begins to emerge, as shown in Fig. 5(h) at $N = 11,000$ for example. This drop in the ZGV frequency pursues until the specimen fails after about 12,500 cycles, and can be explained by the drop in elastic stiffnesses [50–53] and the interaction between the ZGV resonance and the presence of dislocations/cracks in the specimen [28,54–56].

4.2. Discussion of the measured spatial distribution

To analyze the experimental results, the spatial distributions of the variation of the ZGV frequency (depicted by the purple dashed lines in Fig. 5) are plotted on the same graph in Fig. 6 for the measurements
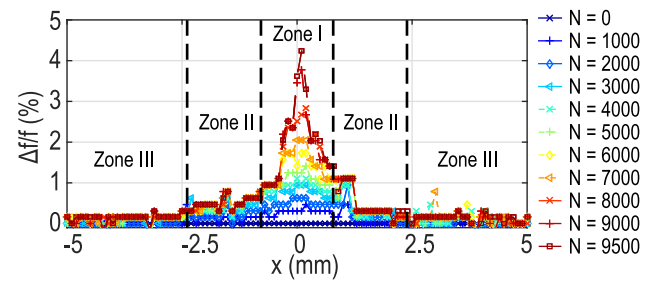

Fig. 6. Experimental measurements of the spatial distribution of the ZGV resonance frequency for different fatigue cycles ($N = 0, 1000, 2000, \ldots 9000, 9500$) and their qualitative classification in three regions.

done from 0 cycle to 9500 cycles, i.e. before the drop of the ZGV frequency. From Fig. 6, the spatial distributions could be qualitatively split into three zones. The zone I in the central part, where the gradient of the frequency variations is the largest, could be mainly associated to the cumulative damage. The zone II, up to about 2.5 mm from the center, where the gradient of the variations is smaller than in the zone I, could be associated to the influence of the residual buckling stress. The zone III, away from the fatigued region, shows mainly an offset of the ZGV resonance frequency (no matter the lateral position $|x| > 2.5$ mm), which may be caused by the traction applied to the specimen when it is unloaded and straightened in order to obtain a flat surface for allowing a good acousto-optic detection during the spatial scanning measurements. The whole spatial distribution will be modeled in Section 5.1 based on these observations and will be proposed to be a weighted sum of respectively a narrow Gaussian function (to account for large gradient of variations), a cosine function, since the residual buckling stress is a cosine function [see Eq. (3)], and an offset. To further analyze the previously-mentioned increase of the ZGV frequency in the center of the scanned area (also seen in Fig. 6), a direct observation of that area under an optical microscope was performed.

4.3. Observation of a specimen during the fatigue test under an optical microscope

For a better understanding of the progression and existence of the fatigue damage, we prepared another aluminum specimen with a similar size in order to take photos with a light microscope during the fatigue test until the failure. Considering that the fatigue crack exists just before the fracture and that the crack propagates very rapidly under fatigue loading after its existence, we choose to decrease the loading compression distance in order to increase our chances to capture the fatigue crack emergence. The loaded compression length is thus decreased to be $2\Delta L = 3$ mm (instead of 5 mm), and the number of fatigue loading cycles before failure in this case is about ~33,000 loading cycles. Three chosen photos are presented in Fig. 7(a–c), which are the top-view on the surface of the specimen after (a) 30,000 cycles, (b) 32,000 cycles, and (c) 33,000 cycles. In Fig. 7(a) and (b), an evident damage is seen in the center of the photos as a brighter zone than the surrounding material. Note that, while dark vertical line within the bright zone and corresponding to micro-crack are barely visible after 30,000 cycles [see Fig. 7(a)], the specimen shows a clearly visible open crack with a very narrow width after 32,000 cycles [see Fig. 7(b)], i.e. just some few cycles before its failure. In Fig. 7(c), the photo after the specimen broke into two pieces is shown. From Fig. 7(a–c), it is very clear that there exists a visible vertical damage area (visible width of about 100 μm) in the center of the photos caused by the accumulation of the buckling induced fatigue.

A fourth photo [see Fig. 7(d)] shows the side-view of the broken specimen. The decrease of the thickness in the middle of the tested specimen can be clearly observed. A zoomed image is also presented
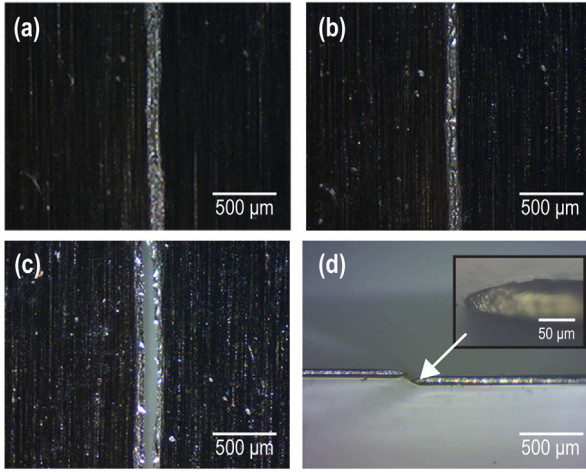
Fig. 7. Top-view optical microscope photos of the fatigue progression on a specimen at (a) 30,000 cycles, (b) 32,000 cycles, and (c) ~33,000 cycles (specimen failure). (d) Side-view of the broken specimen after 33,000 cycles under optical microscope showing symmetrical decrease of the thickness around the fracture.

in the inset of Fig. 7(d), showing an evident symmetrical decrease of the thickness along the normal-to-the-plate-surface direction. Similar features were also observed post-mortem for the first samples. Following this observation, our proposal in the following is to assume that the decrease of the local thickness in the fatigued region completely explains the experimentally-observed increase of the ZGV frequency. This strong, and obviously inaccurate, assumption is done to analyze up to which level of fatigue it remains true. We do assume though that the observed by us [38] and others [15,51,57] change in thickness is at play first, i.e. before any change in mechanical properties of the plate.

The spatial distribution of the ZGV resonance frequency up to 9500 cycles discussed in the previous section, the above demonstration of a symmetrical decrease of the thickness around the crack location and the above-discussed assumption are now used for the construction of an empirical model of the thickness variation with respect to the number of cycles N. This model will in turn be used in a numerical model for frequency–wavenumber (f–k) analysis of the Lamb waves, as detailed in the next Section 5, and for the analysis of the assumption by comparison with the measurements.

5. Empirical model and numerical analyzes

To analyze the influence of the local variation of the plate thickness on the Lamb modes in general, and on the ZGV Lamb mode in particular, it is here proposed to develop a numerical model. The empirical model of the thickness distribution of the plate takes into account the variation of the thickness in the (x, z) plane and is independent of y owing to the symmetry imposed by the fatigue configuration [see Eq. (3)]. In this section, we first introduce the empirical model of the evolution of the thickness distribution with the loading cycles. This model is based on the cumulative fatigue damage theory. The mathematical expression of the thickness distribution is then used for the numerical simulations, the results of which are analyzed and eventually compared to the experimental results discussed in Section 4.

Please note that the circular logic is at play in this section. We indeed assume that the thickness variation explains the whole experimentally-observed variations of the ZGV frequency in order to derive the empirical model, although it is obviously not the case since other material properties are also changing. We do believe though that this is the major ingredient explaining the experimental observation up to a certain level of fatigue. Once more and to be clear, the aim

of this assumption is to reveal that all experimental results cannot be explained only by the thickness variation and to discuss from which fatigue stage must other material changes be considered.

5.1. Empirical model

The numerous empirically- or analytically-based theories of cumulative fatigue damage provide different definitions of the local damage index D depending on the observable and observed parameter. Following the above-discussed experimental observations, it is here proposed to relate the definition of D to the variation of the cross-section, i.e. to the thickness variation, of the specimen under repeated loading. For each spatial position of the measurements, the decrease of the local cross section is equal to the product of the local variation of the thickness $[2h(N, x) - 2h(0, x) = 2\Delta h(N, x) \leq 0]$ and the differential of the variable y (dy). Note that when the sample is intact ($N = 0$), $\Delta h(0, x)$ is zero for all x. For a given number of loading cycles N, the remaining local cross section of the specimen is denoted as $\widetilde{A}(N, x) = 2[h(0, x) + \Delta h(N, x)]dy$. Then, the experimental local damage index $\widetilde{D}(N, x)$ is proposed to be defined as follows:

$$\widetilde{D}(N, x) = \frac{\widetilde{A}(N, x) - \widetilde{A}(0, x)}{\widetilde{A}(0, x)} = \frac{\Delta h(N, x)}{h(0, x)}. \tag{4}$$

Note that, since $\Delta h(N, x)/h(0, x)$ decreases from 0 (intact sample) to -1 (critically damaged sample) as N increases, so is the damage index $\widetilde{D}$. According to Eq. (1) and our assumption, the chosen experimental local damage index is therefore equal to the opposite of the ratio of the ZGV resonance frequency variation $[\Delta f(N, x)]$ to the ZGV frequency when the sample is intact $[f_{ZGV}(0, x)]$:

$$\widetilde{D}(N, x) = -\frac{f_{ZGV}(N, x) - f_{ZGV}(0, x)}{f_{ZGV}(0, x)}$$
$$= -\frac{\Delta f(N, x)}{f_{ZGV}(0, x)}. \tag{5}$$

Since the proposed experimental local damage index $\widetilde{D}(N, x)$ is related to the local relative variation of the plate thickness, it is now proposed to formulate a theoretical model of the damage index, denoted D, based on the fatigue theory, in order to have at hand an empirical model of $\Delta h(N, x)/h(x)$ to implement in the numerical model discussed in the next Section 5.2. The theoretical damage index $D(N, x)$ is proposed to be the sum of three terms corresponding to the three different influences discussed in Section 4.2:

$$D(N, x) = -\left[a_c D_c(N, x) + a_b D_b(N, x) + a_t D_t(N)\right], \tag{6}$$

where a_c, a_b, and a_t stand for constant coefficients allowing the overall balance between the contribution of D_c, D_b, and D_t, respectively, to the theoretical damage index D. Note that the minus sign in front of the square brackets in Eq. (6) stands for the fact that D is imposed to be negative, since $\widetilde{D}$ is negative. Three origins of the fatigue damage are considered in the theoretical model: (i) D_c that accounts for the cumulative damage (using the Lemaitre–Plumtree rule [15,50,51]), (ii) D_b that accounts for the global damage induced by the buckling-caused residual stress, and (iii) D_t that accounts for the global traction applied to the specimen during the LU measurements (necessity of a flat surface, see Section 3). For D_b and D_t, the Miner-linear damage hypothesis [13,15] is considered to model their linear dependence on N. The expression of the theoretical damage index $D(N, x)$ is proposed to be (see Supplemental Material Note 1 for details):

$$D(N, x) = -\left\{ a_c \left[1 - \left(1 - \frac{N}{N_f}\right)^{1/(1+P_N)} \right] \right.$$
$$\times \exp\left[-4\ln 2 \frac{(x - \Delta x)^2}{\sigma^2} \right]$$
$$\left. + a_b \frac{N}{N_f} \left| \cos\left(\pi \frac{x - \Delta x}{L + \delta l}\right) \right| + a_t \frac{N}{N_f} \right\}, \tag{7}$$
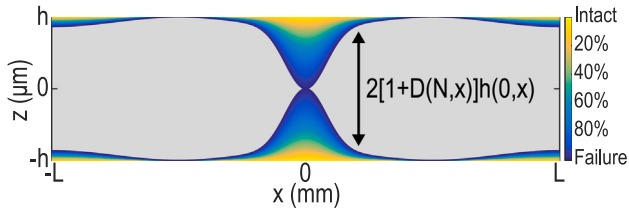
Fig. 8. Illustration of the change in the specimen profiles caused by the fatigue damage. The gray background represents the remaining section of the plate after N_f fatigue cycles and the different color shades stand for the profile evolution of the plate subjected to fatigue damage: from the intact situation (light yellow) to the failure (dark blue) as indicated by the color bar. Numerical values of the input parameters for the calculation are: $P_N = 50$, $\sigma = 1$ mm, $\Delta x = 0$ mm, $2L = 25$ mm, $\delta l = 0.1$ mm, $a_c = 0.98$, $a_b = a_t = 0.01$, and the ratio $N/N_f \in [0\%, 100\%]$. (For interpretation of the references to color in this figure legend, the reader is referred to the web version of this article.)

where N_f is the number of cycles to produce a critical amount of damage (as outlined in Ref. [14]) and P_N, a dimensionless quantity, represents the damage exponent which depends on the plastic strain amplitude; δl stands for the elongation of the specimen due to the traction (assumed to be the same for all unloading) and the absolute value accounts for the fact that, whether the loading stress is positive or negative, it contributes to the damage the same way. Note that, at the center of the fatigue zone ($x = \Delta x$), D_c, D_b, and D_t equal to 1 for $N = N_f$, meaning that $D(N_f, \Delta x) = -(a_c + a_b + a_t)$. Since the minimum of D is -1 according to the chosen definition of the experimental local damage index $\widetilde{D}$, the sum of the three coefficients is therefore imposed to be equal to 1. Assuming that $\widetilde{D} = D$, the thickness distribution of the plate after N loading cycles therefore reads:

$$2h(N, x) = 2[1 + D(N, x)]h(0, x). \tag{8}$$

Using Eq. (8), an illustration of the influence of the fatigue damage on the plate thickness is proposed in Fig. 8, where the following numerical values of the parameters are used: $P_N = 50$, $\sigma = 1$ mm, $\Delta x = 0$ mm, $2L = 25$ mm, $\delta l = 0.1$ mm, $a_c = 0.98$, $a_b = a_t = 0.01$, and the ratio $N/N_f \in [0\%, 100\%]$. The color shades in Fig. 8 stand for the profile evolution of the plate subjected to fatigue damage: from the intact situation (light yellow) to the failure (dark blue) as indicated by the color bar. Note that the damaged profiles on the top and the bottom sides of the plate (see Fig. 8) look well appropriate to match the experimental observations of the distribution of the relative variation of the thickness [see Fig. 7(d)], at least up to a certain amount of fatigue cycles. Now that the model of the evolution of the thickness distribution of the plate with the number of loading cycles has been established, it is proposed to look for the parameters of that model to use in the numerical modeling of the next section. The parameters of the theoretical model to use are the ones that would allow the best fitting of the theoretical damage index D to the experimental damage index $\widetilde{D}$. The known parameters were fixed as follows: $N_f = 12,500$, $\Delta x = 0.1$ mm, and $2L = 25$ mm. The recovery of all the other parameters in Eq. (7) is therefore achieved by minimizing the quadratic relative differences between $\widetilde{D}$ and D as shown in the following cost function $\mathcal{F}$, under the constraints that $a_c + a_b + a_t = 1$:

$$\mathcal{F}(P_N, \sigma, \delta l, a_c, a_b, a_t) = \sum_N \sum_x \left\| \widetilde{D}(N, x) - D\left(N, x, P_N, \sigma, \delta l, a_c, a_b, a_t\right) \right\|^2. \tag{9}$$

The minimization is performed under constraints with the Nelder–Mead simplex algorithm by using the Matlab function @*fminsearch*. After the inverse estimation from Eq. (9), the unknown parameters are determined: $P_N = 44.37$, $\sigma = 0.58$ mm, $\delta l = 0.1$ mm, $a_c = 0.99$, $a_b = 0.004$, and $a_t = 0.006$. We note here that the minimization is done by considering only $N \in [0, 9500]$ cycles, because the proposed model
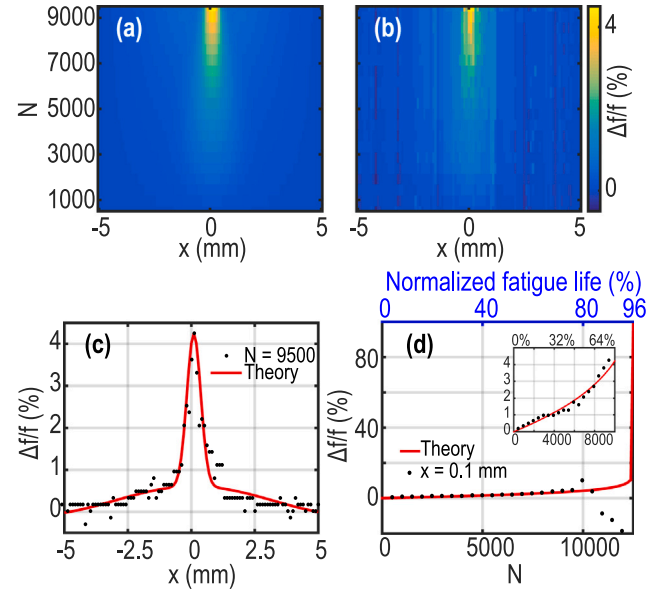

Fig. 9. Comparison between theoretical model and experimental results: (a) distribution of theoretically calculated $\Delta f/f$ as a function of the number of loading cycles N and of the lateral position x; (b) distribution of experimental $\Delta f/f$ as a function of the number of loading cycles N and of the lateral position x; (c) comparison between experimental results and the theoretical fitting after 9500 fatigue cycles; (d) theoretical and experimental evolution of $\Delta f/f$ in the center of the fatigued region (at $x = \Delta x = 0.1$ mm) as a function of the number of loading cycles N.

accounts exclusively for the thickness change that cannot explain the drop of the ZGV frequency. In Fig. 9, the spatial distribution of the relative variation of the ZGV frequency $\Delta f/f$ is plotted as a function of the number of fatigue loading cycles for: (a) the theoretical case using the previously determined parameters and assuming that $\Delta f/f$ is equal to $-D$ [Eq. (7)] and (b) the experimental case. The comparison between the theory (solid lines) and the experimental measurements (points) for two specific cases, i.e. the spatial distribution of $\Delta f/f$ at $N = 9500$ and the evolution of $\Delta f/f$ as a function of loading cycles in the center of the fatigued zone ($x = \Delta x = 0.1$ mm) are also illustrated in Fig. 9(c)–(d), respectively. From Fig. 9(a–c) and as expected for a good inverse estimation, a good agreement is found between the experimental results and the opposite of the cumulative fatigue damage index. In Fig. 9(d), the experimental measurements and the theoretical calculations agree well for $N \in [0, 9500]$, as shown in the inset. After $N = 9500$, the solid red line (theory) is separated and continues to increase where the experimental values decrease since the empirical model only accounts for the thickness variation. For details on the large amount of other theoretical models of cumulative damage which go beyond the scope of this paper, readers are referred to the following reviews/articles [14,15,50,51] and also to the references in these publications. Even if an analysis of the sensitivity of the empirical model to the different variables could be of interest, we believe that such a deep analysis of the sensitivity is out of the scope of this paper, since our aim is to show that all experimental results cannot be explained only by the thickness variation.

In the frame of our hypothesis and empirical model, if one computes the contribution of each term in Eq. (6) to the total damage index for a given number of cycles, it could be noted that: (i) at the center of the fatigue zone and up to 80% of the fatigue lifetime, the contribution of D_b (residual stress) still stands for 7% of the total damage index and that of D_t (traction) for 11%; (ii) at about 1 mm away from the center and up to 80% of the fatigue lifetime, the main contribution is D_t as D_c (cumulative fatigue) drops to 0 and D_b continuously decreases from the center to $x \sim L/2$ and then increases to reach at $x = L$ the same level as at the center. It is therefore concluded that the residual stress and
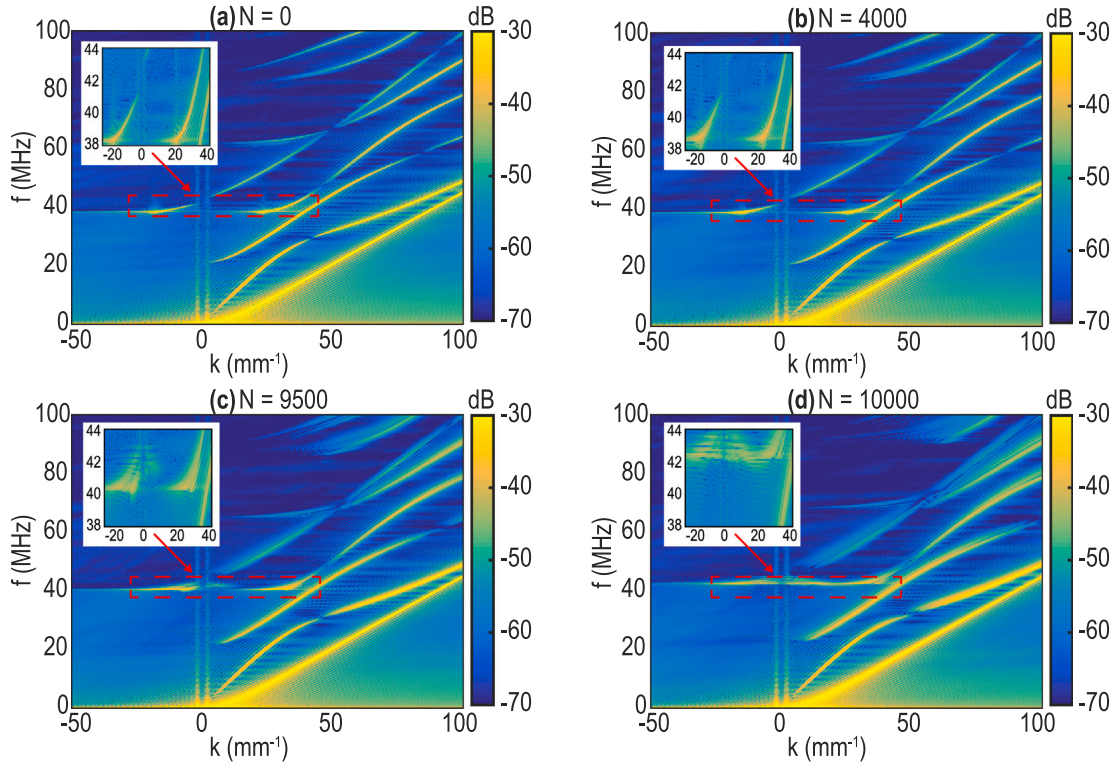
Fig. 10. f–k diagram for the analyzes of the Lamb modes propagating in (a) an intact plate and (b–d) a damaged plate calculated from a set of 376 temporal signals with a spatial scanning step of 10 μm from $x = 0$ mm to $x = L_{num} = 3.75$ mm. Each temporal signal is calculated for a duration of 5 μs with a time step of 1 ns.

the traction contribute equivalently to the damage of the plate away from the center of the fatigue zone.

In the following, the model is supposed to correctly depict the fatigue-based thickness change of the plate. It is now proposed to use the theoretical expression of the plate thickness distribution $2h(N, x)$ [Eq. (8)] to define the geometry of the fatigued plate in a numerical model and to perform frequency–wavenumber (f–k) analyzes of the Lamb modes in such a fatigued sample.

5.2. Numerical model based on finite element method

The numerical calculations to perform f–k analyzes of the Lamb modes in a fatigued sample are realized using the FEM. By considering that our laser beam is focused to a line, the problem is simplified to a two-dimensional problem in the (x, z) plane owing to the symmetry imposed by the source shape. The detailed description of the implemented numerical model is in the Supplemental Material Note 2. The upper and lower surfaces of the two-dimensional model are set to be free. Those upper and lower surfaces in the intact case ($N = 0$) are chosen to be flat and located at $z = +h$ and $z = -h$, respectively, with $2h = 75$ mm. In the cases of the damaged plate, the positions of the upper and lower surfaces are represented by functions of x and of N: $z_{up}(N; x) = +h[1 + D(N; x)]$ and $z_{low}(N; x) = -h[1 + D(N; x)]$, respectively (see the colored profiles in Fig. 8). For a better understanding of the influence of the fatigue damage on the Lamb modes, a set of spatio-temporal signals are probed along the surface profile $z_{low}(N, x)$ of the numerical model. For each damage level (each loading cycles N), 376 numerical signals are saved with a numerical spatial scanning step of 10 μm from $x = 0$ mm to $x = L_{num} = 3.75$ mm. For each saved signal, the duration of the signal is set to be $T_{num} = 5$ μs with a temporal calculation step of 1 ns (i.e. a numerical sampling rate equals to 1 Gs/s). With these simulated calculations (see in Supplemental Material Note 2), it is possible to carry out the two dimensional Fourier transform (2D-FT)

$$\tilde{u}(k, f) = \int_0^{T_{num}} \int_0^{L_{num}} u(x, t) e^{-ikx} e^{i2\pi ft} \mathrm{d}x \mathrm{d}t, \qquad (10)$$

in order to look at the f–k diagram in the real wavenumber plane. The numerical f–k diagram (that corresponds to the dispersion curves only in the intact case) are calculated by the 2D-FT for the four selected cases of different levels of damage in Fig. 10: (a) $N = 0$ [$\Delta h(0, 0)/h(0, 0) = 0\%$], (b) $N = 4000$ [$\Delta h(4000, 0)/h(0, 0) = 1.16\%$], (c) $N = 9500$ [$\Delta h(9500, 0)/h(0, 0) = 3.76\%$], and (d) $N = 10,000$ [$\Delta h(10000, 0)/h(0, 0) = 4.43\%$]. Since the numerical detection is only made in one direction, i.e. in the direction of increasing x (positive group velocities), and since the group velocity and the phase velocity of the S_1 mode are of opposite sign, the phase velocity of S_1 is thus negative. The S_1 wavenumbers are therefore negatives and hence shown in the negative part of the wavenumbers axis ($k < 0$) in Fig. 10(a–d). From these f–k diagram, especially the one in Fig. 10(d), it can be straightforwardly seen, by comparison with the intact case in Fig. 10(a), that the ZGV point is shifted to the right-up side from its original position. It means that both the frequency (f) and the real wavenumber (k) are changed with the kind of local damage that a buckling fatigue test induces to a thin plate.

The information presented in Fig. 10 can be seen as an averaged wave response of the laterally inhomogeneous plate to the photo-excitation in terms of averaged (k, f) characteristics of the acoustic modes. In a non-periodical inhomogeneous plate, these curves of the modes in the (k, f) plane are expected to depend both on the position of the tested region and on its lateral dimension. However, the obtained (k, f) curves are still informative in the sense that their modification with increasing damage (when the position and the dimension of the tested region is fixed) reflects the damage progress and could be applied for its evaluation. The diminishing of the plate thickness should result in the increase of the ZGV frequency, in the diminishing of the wavelength (increasing of the wavenumber) and could qualitatively explain the shift of the ZGV point observed in Fig. 10 with increased fatigue.

Another noticeable feature in Fig. 10 is the increase of the curves width with the progression of damage. This effect could be qualitatively associated to the inhomogeneous broadening of the spectral lines.

Actually, it can be precisely related to inhomogeneous broadening for the acoustic modes with a wavenumber much larger than the inverse of the characteristic scale of the plate inhomogeneity, i.e. the lateral dimension of the thickness variation in this case. Indeed, these modes propagate locally like in locally-homogeneous plates with modified parameters (geometrical acoustic approximation) and their spectral lines broadening could be obtained by spatial averaging of the local spectral lines. However, for waves with wavenumbers smaller than the inverse of the inhomogeneity characteristic scale, the observed broadening could be much more complicated to evaluate quantitatively because the structure of the mode having wavelengths comparable to the scale of the inhomogeneity could be modified. Furthermore, another remarkable phenomenon is observed: a short branch of dispersion curve with negative group velocity appears for small $k_r > 0$ just above the first ZGV frequency and below the corresponding cutoff frequency of the same branch, as seen in the inset of Fig. 10(d). A similar phenomenon is also seen in Fig. 10(c), although much weaker. At present, we attribute these features to the increased scattering of the Lamb waves at the inhomogeneity of the plate.

The comparison between the theoretical model, experimental measurements and numerical validation in the center of the fatigued region ($x = 0$) is plotted in Fig. 11(a) as a function of N, where N is chosen to remain below 10,000, i.e. N is in the range where, experimentally, $\Delta f / f$ only increases and where it is assumed that only the thickness profile change is at play. The solid line represents the theoretical variation of $\Delta f / f$ calculated by the Eq. (7) at $x = 0$ mm. The circles represent the variation of $\Delta f / f$ extracted from the FT of the temporal signal simulated at $x = 0$ mm for $N \in [0, 10000]$ (simulations run every 500 loading cycles). The error bars in Fig. 11(a) stand for $f(N)/[f(0)Q(N)]$, with $f(N)$ the ZGV frequency at $x = 0$ mm after N cycles and $Q(N)$ the quality (Q) factor of the corresponding resonance. Note that the Q factor is defined as $Q = f/(f_2 - f_1)$, where f is the ZGV resonance frequency at which the gain is maximum and f_2 and f_1 are the frequencies higher and lower than f at which the gain is -6 dB than the maximum. From Fig. 11(a), a good agreement between the experimental, the theoretical and the numerical calculations is shown, where the slight discrepancy could be explained by numerical errors/approximations. This validates the numerical model since it reproduces the experimentally-observed relative increase of the ZGV frequency up to 9500 cycles, as expected and assumed.

To go on with the analysis, the numerical Q factors are compared to the experimental Q factors and plotted as a function of N (or normalized fatigue lifetime N/N_f) in Fig. 11(b). The results shown in Fig. 11(b) are twofold. First, the experimental and numerical Q factors match well for $N \in [0, 3500]$ cycles ($N/N_f \in [0, 32]\%$) and this demonstrates a decrease in the Q factor of the ZGV resonance as N increases, i.e. as the thickness change due to the increasingly-pronounced fatigue damage. Second, a linear downward trend of the Q factor is particularly evident in our model where other changes of the material (damping property, mechanical property, …) are not considered, whereas an abrupt decrease of the experimental Q factor is observed from $N = 3500$ to $N = 4000$.

These observations lead to three important comments to point out: (i) no damping factor is considered in this numerical model, while the Q factor decreases as N increases, both for simulations and experiments, meaning that the attenuation of the resonance can be only influenced by the local geometry of the plate; (ii) the good match between the simulations and the experimental measurements confirms that our proposed empirical model describes well the fatigue process at the early stage of the fatigue life ($N/N_f < 32\%$); (iii) the drop of the experimental Q factor at $N = 4000$ and the change of the decreasing slope after that, could be the interesting manifestation of the start of the changes in the material elastic parameters (see Supplemental Material Note 3 for the reproducibility of this observation). We have therefore demonstrated here that the experimentally-observed increase of the ZGV frequency is not only due to the thickness decrease of the
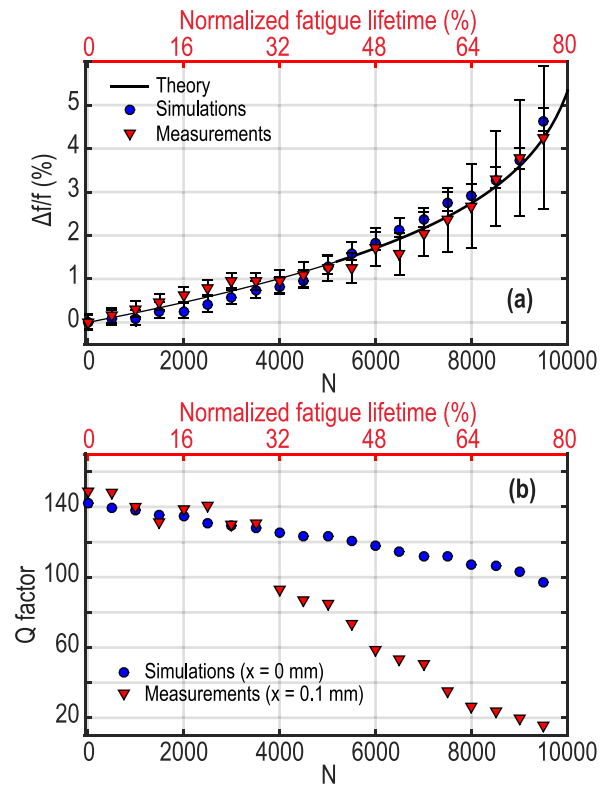

Fig. 11. (a) Theoretical (solid line), experimental (triangles) and numerical evolution (circles) of the relative variation of the ZGV frequency at the center of the fatigued region as a function of the loading fatigue cycles N; (b) Comparison of the experimental (triangles) and the numerical (circles) Q factors as a function pf N.

fatigued plate, since this assumption does not allow reproducing both the frequency value increase and the Q factor drop. In particular, we have seen that the changes of mechanical properties cannot be ignored anymore after 30% of the fatigue lifetime.

6. Concluding remarks

This paper analyzes along several lines a non-contact LU evaluation of cumulative fatigue damage in thin solid plates by monitoring a ZGV resonance frequency. For better understanding of the evolution of the thickness distribution in the specimen during fatigue test and of its effect on the ZGV resonance frequency, an empirically-based theoretical model is proposed. It describes the evolution of the thickness distribution with the cumulative fatigue damage. A numerical model, based on FEM, allows the frequency–wavenumber (f–k) analyzes of the Lamb modes in fatigued metal plates.

The developed theoretical model have shown a good agreement with the experimental results (frequency value and Q factor) up to a certain amount of fatigue damage, which allows assuming that the change in the thickness distribution due to the cumulative thickness variations is at major play up to 30% of the fatigue lifetime. The last comparison between the quality factor of the ZGV resonance calculated from the numerical simulations and from the experimental results has indeed shown that the experimentally-observed dramatic drop of the Q factor after 30% of the fatigue lifetime cannot be explained by the change in the thickness distribution. The start time of the change of mechanical properties during the early fatigue stage is therefore expected to be more easily identified with the Q factor of the ZGV resonance than with its frequency. The current model only accounting for the fatigue-based thickness variation does not capture all involved processes. Thus, a more complete model should be developed in the

future to take into account the change in the mechanical properties as the fatigue damage increases, which could also allow predicting the abrupt decrease of the ZGV resonance frequency.

For future works, we will focus on the imaging of the fatigue damage for analyzing the limits and the capacities of the presented method, especially at few loading cycles and with varieties of cumulative damage tests, when the damage is barely visible. Thanks to the potential of the presented method for quantitative prediction of fatigue progress, the assessment of fatigue damage in different stages, especially before the specimen failure, could be achieved by combining the proposed method with either chemical methods (such as etch-pit technique [58] and precipitation technique [2]) or physical techniques (such as transmission electron microscopy [56] or X-ray diffraction technique [59]). The achievement of this challenging prospect would further reveal the nature of such damage and would help identifying the material mechanisms leading to the observed extremum in the ZGV resonance frequency to eventually have at hand a fully quantitative (local) damage evaluation method for fatigued samples.

CRediT authorship contribution statement

Declaration of competing interest

The authors declare that they have no known competing financial interests or personal relationships that could have appeared to influence the work reported in this paper.

Acknowledgments

Appendix A. Supplementary data

Supplementary material related to this article can be found online at https://doi.org/10.1016/j.ndteint.2020.102323.

References

[1] Kennedy AJ. A new detection of fatigue damage in metals. Nature 1957;179:1291–2. http://dx.doi.org/10.1038/1791291a0.

[2] Dieter G. Mechanical metallurgy. Metallurgy and metallurgical engineering series, McGraw-Hill; 1961.

[3] Stephens R, Fatemi A, Stephens R, Fuchs H. Metal fatigue in engineering a Wiley-Interscience Publication. John Wiley & Sons; 2000.

[4] Kruzic JJ. Predicting fatigue failures. Science 2009;325:156–8. http://dx.doi.org/10.1126/science.1173432.

[5] Dowling N, Prasad K, Narayanasamy R. Mechanical behavior of materials: engineering methods for deformation, fracture, and fatigue, always learning. Pearson; 2012.

[6] Schijve J. Fatigue of structures and materials in the 20th century and the state of the art. Int J Fatigue 2003;25:679–702. http://dx.doi.org/10.1016/S0142-1123(03)00051-3.

[7] Withers PJ. Residual stress and its role in failure. Rep Progr Phys 2007;70:2211–64. http://dx.doi.org/10.1088/0034-4885/70/12/R04.

[8] Kumar A, Torbet CJ, Pollock TM, Wayne Jones J. In situ characterization of fatigue damage evolution in a cast al alloy via nonlinear ultrasonic measurements. Acta Mater 2010;58:2143–54. http://dx.doi.org/10.1016/j.actamat.2009.11.055.

[9] Kang T, Kim H-H, Song S-J, Kim H-J. Characterization of fatigue damage of al6061-t6 with ultrasound. NDT E Int 2012;52:51–6. http://dx.doi.org/10.1016/j.ndteint.2012.08.001.

[10] Bak BLV, Sarrado C, Turon A, Costa J. Delamination under fatigue loads in composite laminates: A review on the observed phenomenology and computational methods. Appl Mech Rev 2014;66:060803. http://dx.doi.org/10.1115/1.4027647.

[11] Pineau A, McDowell DL, Busso EP, Antolovich SD. Failure of metals ii: Fatigue. Acta Mater 2016;107:484–507. http://dx.doi.org/10.1016/j.actamat.2015.05.050.

[12] Kamal M, Rahman MM. Advances in fatigue life modeling: A review. Renew Sust Energ Rev 2018;82:940–9. http://dx.doi.org/10.1016/j.rser.2017.09.047.

[13] Miner M. Cumulative damage in fatigue. J Appl Mech 1945;12:A159–64.

[14] Lemaitre J, Plumtree A. Application of damage concepts to predict creep-fatigue failures. J Eng Mater Technol 1979;101:284–92. http://dx.doi.org/10.1115/1.3443689.

[15] Fatemi A, Yang L. Cumulative fatigue damage and life prediction theories: a survey of the state of the art for homogeneous materials. Int J Fatigue 1998;20:9–34. http://dx.doi.org/10.1016/S0142-1123(97)00081-9.

[16] Yang L, Fatemi A. Cumulative fatigue damage mechanisms and quantifying parameters: A literature review. J Test Eval 1998;26:89–100. http://dx.doi.org/10.1520/JTE11978J.

[17] Nagy PB. Fatigue damage assessment by nonlinear ultrasonic materials characterization. Ultrasonics 1998;36:375–81. http://dx.doi.org/10.1016/S0041-624X(97)00040-1.

[18] Deng M, Pei J. Assessment of accumulated fatigue damage in solid plates using nonlinear lamb wave approach. Appl Phys Lett 2007;90:121902. http://dx.doi.org/10.1063/1.2714333.

[19] Jaya Rao VVS, Kannan E, Prakash RV, Balasubramaniam K. Fatigue damage characterization using surface acoustic wave nonlinearity in aluminum alloy aa7175-t7351. J Appl Phys 2008;104:123508. http://dx.doi.org/10.1063/1.2956396.

[20] Pruell C, Kim J-Y, Qu J, Jacobs LJ. Evaluation of plasticity driven material damage using lamb waves. Appl Phys Lett 2007;91:231911. http://dx.doi.org/10.1063/1.2811954.

[21] Tam AC. Applications of photoacoustic sensing techniques. Rev Modern Phys 1986;58:381–431. http://dx.doi.org/10.1103/RevModPhys.58.381.

[22] Scruby C, Drain L. Laser ultrasonics techniques and applications. Taylor & Francis; 1990.

[23] Chigarev N, Tournat V, Gusev V. All-optical monitoring of acoustic waves guided by confined micro-fluidic layers. Appl Phys Lett 2012;100:144102. http://dx.doi.org/10.1063/1.3701576.

[24] Mezil S, Chigarev N, Tournat V, Gusev V. Evaluation of crack parameters by a nonlinear frequency-mixing laser ultrasonics method. Ultrasonics 2016;69:225–35. http://dx.doi.org/10.1016/j.ultras.2016.04.005.

[25] Bermes C, Kim J-Y, Qu J, Jacobs LJ. Experimental characterization of material nonlinearity using lamb waves. Appl Phys Lett 2007;90:021901. http://dx.doi.org/10.1063/1.2431467.

[26] Cantrell JH, Yost WT. Nonlinear ultrasonic characterization of fatigue microstructures. Int J Fatigue 2001;23:487–90. http://dx.doi.org/10.1016/S0142-1123(01)00162-1.

[27] Pruell C, Kim J-Y, Qu J, Jacobs LJ. Evaluation of fatigue damage using nonlinear guided waves. Smart Mater Struct 2009;18:035003. http://dx.doi.org/10.1088/0964-1726/18/3/035003.

[28] Pyrak-Nolte LJ, Xu J, Haley GM. Elastic interface waves propagating in a fracture. Phys Rev Lett 1992;68:3650–3. http://dx.doi.org/10.1103/PhysRevLett.68.3650.

[29] Prada C, Balogun O, Murray TW. Laser-based ultrasonic generation and detection of zero-group velocity lamb waves in thin plates. Appl Phys Lett 2005;87:194109. http://dx.doi.org/10.1063/1.2128063.

[30] Clorennec D, Prada C, Royer D, Murray TW. Laser impulse generation and interferometer detection of zero group velocity lamb mode resonance. Appl Phys Lett 2006;89:024101. http://dx.doi.org/10.1063/1.2220010.

[31] Clorennec D, Prada C, Royer D. Laser ultrasonic inspection of plates using zero-group velocity lamb modes. IEEE Trans Ultrason Ferroelectr Freq Control 2010;57:1125–32. http://dx.doi.org/10.1109/TUFFC.2010.1523.

[32] Prada C, Clorennec D, Royer D. Power law decay of zero group velocity lamb modes. Wave Motion 2008;45:723–8. http://dx.doi.org/10.1016/j.wavemoti.2007.11.005.

[33] Prada C, Clorennec D, Royer D. Local vibration of an elastic plate and zero-group velocity lamb modes. J Acoust Soc Am 2008;124:203–12. http://dx.doi.org/10.1121/1.2918543.

[34] Raetz S, Laurent J, Dehoux T, Royer D, Audoin B, Prada C. Effect of refracted light distribution on the photoelastic generation of zero-group velocity lamb modes in optically low-absorbing plates. J Acoust Soc Am 2015;138:3522–30. http://dx.doi.org/10.1121/1.4936903.

[35] Prada C, Clorennec D, Murray TW, Royer D. Influence of the anisotropy on zero-group velocity lamb modes. J Acoust Soc Am 2009;126:620–5. http://dx.doi.org/10.1121/1.3167277.

[36] Mezil S, Bruno F, Raetz S, Laurent J, Royer D, Prada C. Investigation of interfacial stiffnesses of a tri-layer using zero-group velocity lamb modes. J Acoust Soc Am 2015;138:3202–9. http://dx.doi.org/10.1121/1.4934958.

[37] Faëse F, Raetz S, Chigarev N, Mechri C, Blondeau J, Campagne B, et al. Beam shaping to enhance zero group velocity lamb mode generation in a composite plate and nondestructive testing application. NDT & E Int 2017;85:13–9. http://dx.doi.org/10.1016/j.ndteint.2016.09.003.

[38] Yan G, Raetz S, Chigarev N, Gusev VE, Tournat V. Characterization of progressive fatigue damage in solid plates by laser ultrasonic monitoring of zero-group-velocity lamb modes. Phys Rev Appl 2018;9:061001. http://dx.doi.org/10.1103/PhysRevApplied.9.061001.

[39] Balogun O, Murray TW, Prada C. Simulation and measurement of the optical excitation of the s1 zero group velocity lamb wave resonance in plates. J Appl Phys 2007;102:064914. http://dx.doi.org/10.1063/1.2784031.

[40] Cès M, Clorennec D, Royer D, Prada C. Thin layer thickness measurements by zero group velocity lamb mode resonances. Rev Sci Instrum 2011;82:114902. http://dx.doi.org/10.1063/1.3660182.

[41] Clorennec D, Prada C, Royer D. Local and noncontact measurements of bulk acoustic wave velocities in thin isotropic plates and shells using zero group velocity lamb modes. J Appl Phys 2007;101:034908. http://dx.doi.org/10.1063/1.2434824.

[42] Mezil S, Chigarev N, Tournat V, Gusev V. All-optical probing of the nonlinear acoustics of a crack. Opt Lett 2011;36:3449–51. http://dx.doi.org/10.1364/OL.36.003449.

[43] Higuet J, Valier-Brasier T, Dehoux T, Audoin B. Beam distortion detection and deflectometry measurements of gigahertz surface acoustic waves. Rev Sci Instrum 2011;82:114905. http://dx.doi.org/10.1063/1.3660193.

[44] Gasteau D, Chigarev N, Ducousso-Ganjehi L, Gusev VE, Jenson F, Calmon P, et al. Single crystal elastic constants evaluated with surface acoustic waves generated and detected by lasers within polycrystalline steel samples. J Appl Phys 2016;119:043103. http://dx.doi.org/10.1063/1.4940367.

[45] Hutchinson JW. Stresses and failure modes in thin films and multilayers, department of solid mechanics. Denmark: Technical University of Denmark; 1996.

[46] Cotterell B, Chen Z. Buckling and cracking of thin films on compliant substrates under compression. Int J Fract 2000;104:169–79. http://dx.doi.org/10.1023/A:1007628800620.

[47] Lewicka M, Mahadevan L, Pakzad MR. The föppl-von kármán equations for plates with incompatible strains. Proc R Soc Lond Ser A Math Phys Eng Sci 2010;467:402–26. http://dx.doi.org/10.1098/rspa.2010.0138.

[48] Beuth JL. Cracking of thin bonded films in residual tension. Int J Sol Struct 1992;29:1657–75. http://dx.doi.org/10.1016/0020-7683(92)90015-L.

[49] Chai H, Babcock CD. Two-dimensional modelling of compressive failure in delaminated laminates. J Compos Mater 1985;19:67–98. http://dx.doi.org/10.1177/002199838501900105.

[50] Lemaitre J, Dufailly J. Damage measurements. Eng Fract Mech 1987;28:643–61. http://dx.doi.org/10.1016/0013-7944(87)90059-2.

[51] Plumtree A, O'Connor BPD. Damage accumulation and fatigue crack propagation in a squeeze-formed aluminium alloy. Int J Fatigue 1989;11:249–54. http://dx.doi.org/10.1016/0142-1123(89)90308-3.

[52] Barsoum MW, Radovic M, Zhen T, Finkel P, Kalidindi SR. Dynamic elastic hysteretic solids and dislocations. Phys Rev Lett 2005;94:085501. http://dx.doi.org/10.1103/PhysRevLett.94.085501.

[53] Li SJ, Murr LE, Cheng XY, Zhang ZB, Hao YL, Yang R, et al. Compression fatigue behavior of ti-6al-4v mesh arrays fabricated by electron beam melting. Acta Mater 2012;60:793–802. http://dx.doi.org/10.1016/j.actamat.2011.10.051.

[54] Maurel A, Pagneux V, Barra F, Lund F. Wave propagation through a random array of pinned dislocations: Velocity change and attenuation in a generalized granato and lücke theory. Phys Rev B 2005;72:174111. http://dx.doi.org/10.1103/PhysRevB.72.174111.

[55] Mujica N, Cerda MT, Espinoza R, Lisoni J, Lund F. Ultrasound as a probe of dislocation density in aluminum. Acta Mater 2012;60:5828–37. http://dx.doi.org/10.1016/j.actamat.2012.07.023.

[56] Barra F, Espinoza-González R, Fernández H, Lund F, Maurel A, Pagneux V. The use of ultrasound to measure dislocation density. JOM 2015;67:1856–63. http://dx.doi.org/10.1007/s11837-015-1458-9.

[57] Makkonen M. Predicting the total fatigue life in metals. Int J Fatigue 2009;31:1163–75. http://dx.doi.org/10.1016/j.ijfatigue.2008.12.008.

[58] Johnston WG, Gilman JJ, velocities Dislocation, densities dislocation. Dislocation velocities dislocation densities and plastic flow in lithium fluoride crystals. J Appl Phys 1959;30:129–44. http://dx.doi.org/10.1063/1.1735121.

[59] Cullity B, Stock S. Elements of X-ray diffraction. 3rd ed. Prentice-Hall; 2001.